Modulation of *d*-Orbital Interactions in Dual-Atom Catalysts for Enhanced Polysulfide Anchoring and Kinetics in Lithium–Sulfur Batteries

Jianfeng Liu, Qiu He,* Wanjuan Zou, Mingwei Wu, Celso Ricardo Caldeira Rego, Chenxi Xia, Yan Xiong,* and Yan Zhao*

ABSTRACT: Modulating the electronic structure is essential for improving the anchoring and catalytic capabilities of catalysts in lithium–sulfur batteries (LSBs). This study delves into the modulation of *d*-orbitals in transition metal dual-atom catalysts (DACs) supported by boron nitride and graphene (BNC) hybrid sheets for LSBs. This study reveals that the *d*-band center of the DAC s, a key determinant of material chemical properties, is primarily determined by the electronic configuration of the d_{yz} and $d_{x^2-y^2}$ orbitals. Furthermore, the interaction between d_{z^2} of transition metals and S_3 *p* orbitals is critical for the binding strength of LiPSs. By understanding these interactions, the functionality of DACs can be customized for optimal performance in LSBs. For example, the MnCrBNC catalyst with 10 *d*-electrons exhibits the optimal *d*-band center and demonstrates exceptional LiPSs binding capability, the lowest Li_2S decomposition energy barrier, and the lowest Gibbs free energy of reaction for the rate-determining step of sulfur reduction. This study elucidates the fundamental mechanisms for designing high-performance LSB catalysts through electronic structure modulation.

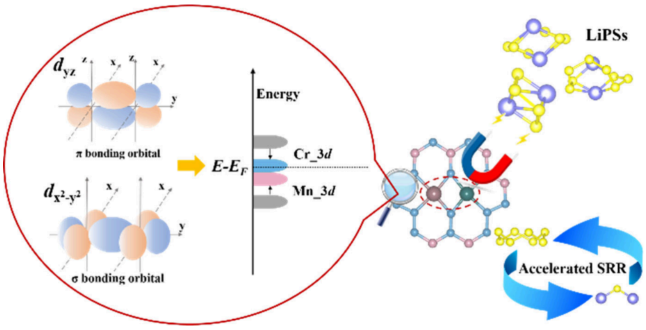

KEYWORDS: *dual-atom catalysts, lithium–sulfur batteries, catalysis, d-band center, electronic structure modulation*

1. INTRODUCTION

The lithium–sulfur battery (LSB) has emerged as a promising energy storage solution poised to replace commercial lithium–ion batteries due to its impressive theoretical capacity of 1675 mAh g^{-1}, the abundance of sulfur cathode resources, and the environmental friendliness of sulfur as a cathode material.[1−4] However, the insulating nature of the sulfur cathode, the lithium polysulfides (LiPSs) shuttle effect, and the sluggish reaction kinetics have significantly hindered its widespread adoption.[5,6] The shuttle effect, involving the highly soluble intermediate product LiPSs (mainly Li_2S_n, $4 \leq n \leq 8$) moving between the electrode through the electrolyte, leads to the depletion of active materials and reduced Coulombic efficiencies.[7−10] Addressing these challenges requires developing multifunctional materials with high conductivity, strong LiPSs anchoring capabilities, and robust catalytic performance. Researchers have identified this strategy as promising yet demanding for overcoming the inherent obstacles LSBs face.[11]

In the past decade, transition metal (TM) single atom catalysts (SACs) have emerged as prominent sulfur host materials for LSBs due to their remarkable catalytic activity, adjustable electronic properties, and maximized atom efficiency.[12−15] The Lewis acid–base interaction between the TM sites and LiPSs enhances the anchoring effect of LiPSs and facilitates charge–discharge reactions within LSB. Studies have shown that SACs weaken and elongate Li–S bonds in Li_2S upon coordination, activating the typically inert Li_2S and aiding its decomposition during the initial charging phase.[16,17] A prevalent SAC design involves anchoring onto an electrically conductive matrix and coordinating with nonmetallic heteroatoms (e.g., N, O, and S) to stabilize the structure. For example, Li's group[18] employed a template approach to fabricate N-doped carbon nanosheets loaded with Co (CoSA-N-C) as cathode modification materials. The isolated Co atoms exhibit a strong affinity for LiPSs, effectively mitigating the "shuttle effect". Furthermore, the N atoms coordinated with the metal atoms accelerate the oxidation of Li_2S, thereby regulating the deposition behavior of Li_2S. In some cases, the metal center and its corresponding nonmetal atoms synergistically contribute to anchoring LiPSs and catalytic effects.[19] Consequently, SACs have significantly enhanced the rate capability and cycling performance of LSBs.

Common strategies for enhancing the catalytic activity of SACs involve introducing geometric defects (local distortion), adjusting coordination numbers, and incorporating heteroatoms.[20−23] However, SACs with only one TM center have limitations in facilitating multistep catalysis. To prevent monatomic aggregation, SACs were usually designed with a low mass loading, resulting in decreased overall activity.[24] On the other hand, due to the specific single active center of SACs, breaking the linear relationship between different intermediate adsorption energies is challenging.[25] As an extension of SACs, dual-atom catalysts (DACs) with high mass loadings and adaptable active sites can leverage the synergistic effects between the dual atoms to bestow novel properties.[26−28] The increase in atomic loading and unique orbital interactions between the two adjacent TM atoms in DACs, enhancing the catalytic performance.[29,30] Chen et al.[31] prepared a Ni−Fe diatomic catalyst pair with a total metal content of 7.29 wt % (twice the number of active sites in SANi/Fe), demonstrating enhanced catalytic performance in CO_2 redox reaction and O_2 evolution. Hu et al.[32] observed the interaction between H and Ru could be modulated by Pt in Pt−Ru dimer, resulting in a notable enhancement in the H_2 evolution reaction activity.

Hexagonal boron nitride (BN) boasts a structure and properties akin to graphene, featuring high specific surface area, excellent thermal conductivity, mechanical robustness, and fire resistance.[33] Despite its structural similarity to graphene, BN exhibits ten times greater ductility. The graphene and BN hybrid nanosheets (BNC) combine the advantages of BN and graphene, enhancing flame retardancy and toughness relative to graphene, thereby reducing the risk of battery spontaneous combustion and significantly boosting safety. Therefore, it is expected to demonstrate outstanding performance in LSB. Moreover, the BNC inherits the exceptional electrical conductivity of graphene. Ci et al.[34] pioneered the synthesis of BNC via chemical vapor deposition, demonstrating the capability to modulate their conductivity by adjusting the atomic percentage of carbon atoms from 10% to 100%. This attribute positions BNC as a promising conductive substrate for DACs in LSB.

This study presents a method for adjusting the *d*-band center in DACs by modifying heteronuclear metal atoms. The setup involved individually and dually doping 3*d* TM atoms into the BNC substrate to form SACs and DACs, respectively. We then conducted first-principles calculations, including the partial density of states (PDOS) and crystal orbital Hamilton population (COHP) analyses, to reveal that orbital interactions between the adjacent TM atoms could influence their d-band center, mainly through the d_{xz} and $d_{x^2-y^2}$ orbitals. Our computational results illustrated that MnCrBNC exhibited superior anchoring of LiPSs and effective mitigation of the shuttle effect due to the regulation of the *d*-band centers of the transition metal sites. Furthermore, the decomposition energy barrier for Li_2S on MnCrBNC was notably low at 1.25 eV, as determined by the climbing image nudged elastic band (CI-NEB) method, signifying enhanced decomposition efficiency compared to SACs. Thermodynamic assessments of the sulfur reduction reaction (SRR) indicated that MnCrBNC showcases an even lower conversion barrier, highlighting its effective facilitation of the kinetics for the LiPS transformations. These findings instill confidence in the effectiveness of our proposed method.

2. COMPUTATIONAL METHODS

All theoretical calculations in this study employed density functional theory (DFT) implemented in the Vienna Ab Initio Simulation Package (VASP).[35,36] For the description of electronic and structural properties, we used the Perdew−Burke−Ernzerhof (PBE) functional within the generalized gradient approximation (GGA).[37,38] To account for van der Waals (vdW) forces in the adsorbate-interface interaction, we employed the DFT-D3 method by Grimme.[39] The Kohn−Sham equations were solved using the projector augmented wave (PAW) method with a cutoff energy of 520 eV. During geometry optimizations, we set convergence criteria for energy and force at 1×10^{-5} eV and 0.02 eV/Å, respectively. A vacuum slab of 20 Å was introduced along the Z direction to eliminate image interactions between two periodic units. Brillouin zone integration was performed using a 2 × 1 × 1 k-point grid for geometry optimization and a 3 × 2 × 1 k-point grid for electronic calculations. Static calculations required a total energy difference of less than 1×10^{-6} eV. To assess thermodynamic stability, we conducted ab initio molecular dynamics (AIMD) simulations. The decomposition barrier of Li_2S was determined utilizing the CI-NEB method.[40]

The defect formation energy is defined as

$$E_f = E_{(\text{defect},q)} - E_{(\text{pure})} \pm \sum \Delta n_x \mu_x \tag{1}$$

where $E_{(\text{defect},q)}$ is the total energy of the substrates with defect, $E_{(\text{pure})}$ is the energy of the substrates without defect, Δn_x is the number of atoms being added or removed, μ_x is the chemical potential which represents the approximated energy of an individual atom.

The surface energy is defined as

$$\sigma = 1/2A(E_{\text{slab}} - NE_{\text{bulk}}) \tag{2}$$

where A is the surface area of the slab, E_{slab} is the energy of of a relaxed slab, N is the ratio of the number of atoms in the slab to the number of atoms in the bulk, and E_{bulk} is the energy of a relaxed bulk.

The adsorption energy (E_{ad}) of each LiPS on substrates was calculated using the following equation:

$$E_{\text{ad}} = E_{\text{substrate}\cdots\text{LiPS}} - E_{\text{substrate}} - E_{\text{LiPS}} \tag{3}$$

where $E_{\text{substrate}\cdots\text{LiPS}}$, $E_{\text{substrate}}$, and E_{LiPS} denote the energies of the adsorption complex of a LiPS molecule on a substrate, the substrate, and the isolated LiPS molecule, respectively.

The contribution ratio of the vdW force (R_{vdW}) to the adsorption was determined using the following formula:

$$R_{\text{vdW}} = (E_{\text{ad}}^{\text{vdW}} - E_{\text{ad}}^{\text{no\_vdW}})/E_{\text{ad}}^{\text{vdW}} \times 100\% \tag{4}$$

where $E_{\text{ad}}^{\text{vdW}}$ and $E_{\text{ad}}^{\text{no\_vdW}}$ represent the adsorption energy with and without D3 vdW energies, respectively. The charge density difference of the substrate···LiPS complex, which describes the electronic interaction of the LiPS adsorbate and the substrate, was calculated using the following equation:

$$\Delta\rho = \rho_{\text{substrate}\cdots\text{LiPS}} - \rho_{\text{substrate}} - \rho_{\text{LiPS}} \tag{5}$$

where $\rho_{\text{substrate}\cdots\text{LiPS}}$, $\rho_{\text{substrate}}$, and ρ_{LiPS} are the charge densities of the substrate···LiPS complex, the substrate, and the isolated LiPS, respectively.

The hydrogen electrode model was utilized to calculate the free energy change for SRR, and the multiple steps from S_8 to Li_2S are listed below, with the molecule denoted by a star "*" representing the adsorbed species.

$$S_8 + 16Li^+ \rightarrow S_8^* + 16Li^+ \ (\Delta G1) \tag{6}$$

$$S_8^* + 16Li^+ + 2e^- \rightarrow Li_2S_8^* + 14Li^+ \ (\Delta G2) \tag{7}$$

$$Li_2S_8^* + 14Li^+ + 2e^- \rightarrow Li_2S_6^* + Li_2S_2 + 12Li^+ \ (\Delta G3) \tag{8}$$

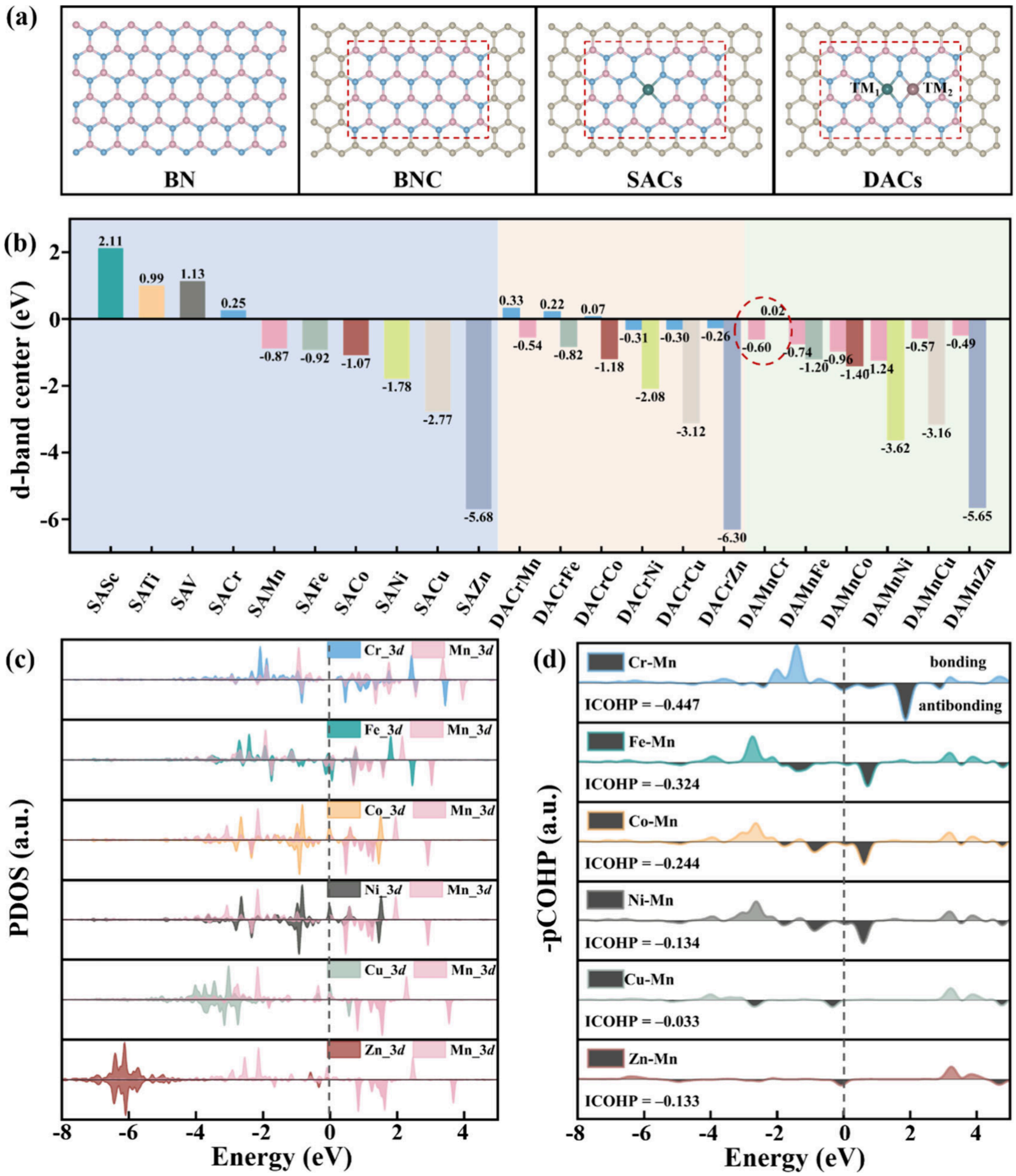

Figure 1. (a) Optimized structures of BN, BNC, SACs, and DACs. (b) The *d*-band centers of TMs in SACs and DACs. The (c) PDOS of dual TMs and (d) COHP of the Mn−TM bond in MnTMBNC.

$$Li_2S_6^* + Li_2S_2 + 12Li^+ + 2e^- \rightarrow Li_2S_4^* + 2Li_2S_2 + 10Li^+ \ (\Delta G4) \qquad (9)$$

$$Li_2S_4^* + 2Li_2S_2 + 10Li^+ + 2e^- \rightarrow Li_2S_2^* + 3Li_2S_2 + 8Li^+ \ (\Delta G5) \qquad (10)$$

$$Li_2S_2^* + 3Li_2S_2 + 8Li^+ + 8e^- \rightarrow Li_2S^* + 7Li_2S \ (\Delta G6) \qquad (11)$$

3. RESULTS AND DISCUSSION

3.1. Electronic Structure Analysis. As shown in Figure 1(a), 10 SACs and 12 DACs were constructed by doping different 3*d* TMs into the BNC nanosheets. The total density of states (TDOSs) were collected in Figure S1 and Figure S2

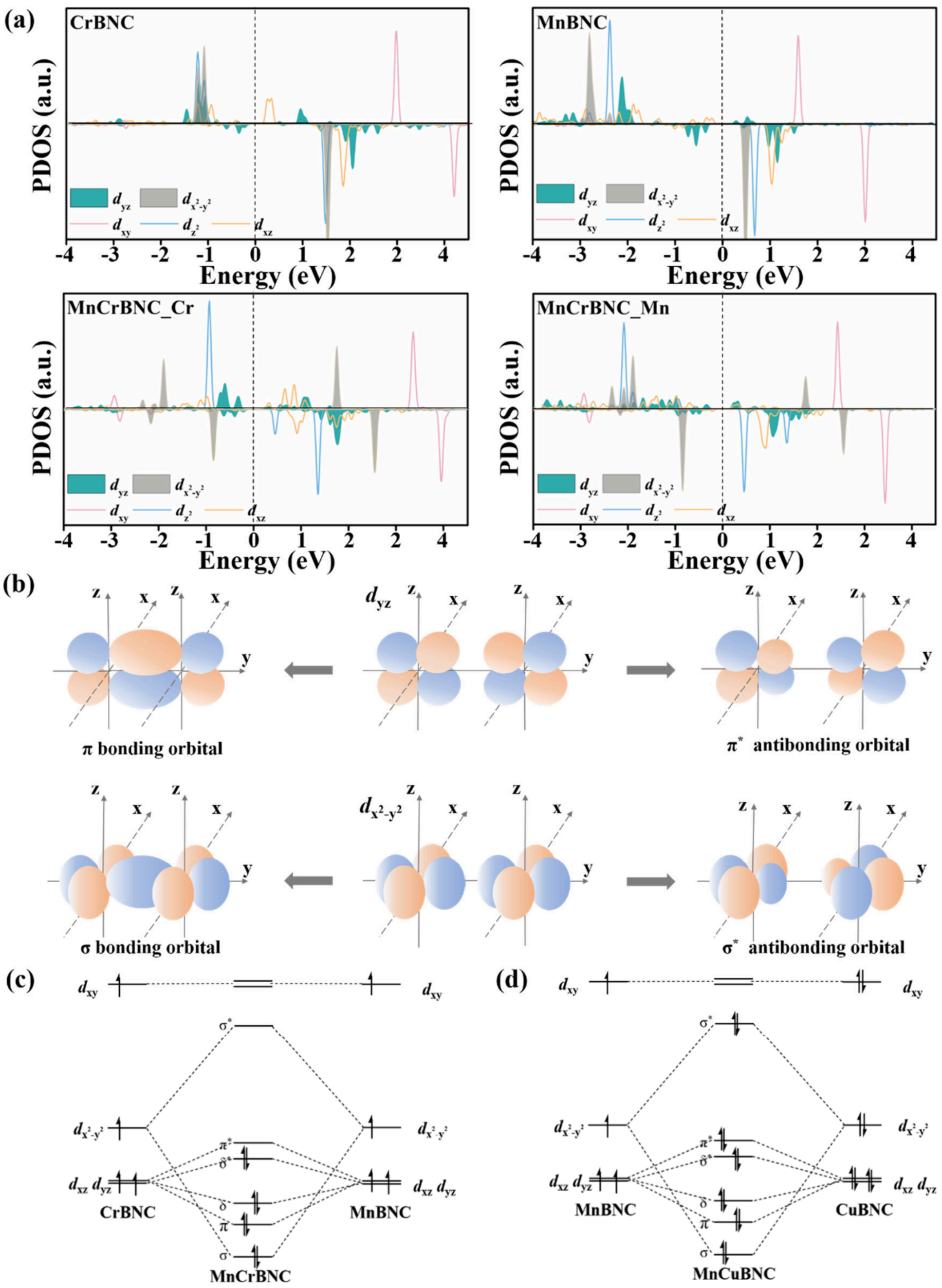

Figure 2. (a) PDOS of Cr and Mn *d*-orbitals in CrBNC, MnBNC, and MnCrBNC. (b) The bonding and antibonding orbital forms of $d_{yz}\_d_{yz}$ and $d_{x^2-y^2}\_d_{x^2-y^2}$. The *d*-orbital interaction diagrams between Mn and TM in (c) MnCrBNC and (d) MnCuBNC.

to show their electronic structures and conductivities. Compared to the pure BNC nanosheets, SACs and DACs significantly reduce the band gap, thereby enhancing the electrical conductivity. The *d*-electrons are typically active in TMs, and the *d*-band center has been shown to be highly relevant to their catalytical activities.[41,42] To elaborate on the synergistic influence of heteronuclear DACs and the distinctions in electronic structure compared to SACs, the *d*-band centers of SACs and DACs were calculated and are presented in Figure 1(b). The *d*-band centers of SACs range from−5.68 to 2.11 eV, with CrBNC (0.25 eV) and MnBNC (−0.87 eV) being the closest to the Fermi level, indicating their potential for high activity. The optimized structures of SACs are depicted in Figure S3, and the Sc, Ti, and V-SACs exhibit distortion along the *z*-axis, which may further aggravate during the adsorption reaction and affect the stability of the structure. Therefore, the Sc, Ti, and V-SACs are excluded for further investigation. Furthermore, to balance computational cost and efficiency, we focused on two categories of heteronuclear DACs: one with fixed Cr and variable atoms (TM = Mn, Fe, Co, Ni, Cu, Zn); the other with fixed Mn and variable atoms (Cr, Fe, Co, Ni, Cu, Zn). The *d*-band centers of Cr in CrTMBNC and Mn in MnTMBNC exhibit a similar trend of variation corresponding to changes in the variable TM atoms. Furthermore, the combination of Cr and Mn in MnCrBNC shifts both their *d*-band centers closer to the Fermi level, suggesting potentially higher activity compared to CrBNC and MnBNC. The variations in the *d*-band centers of the TM atoms in both CrTMBNC and MnTMBNC, in comparison to the corresponding TMBNC SACs, do not follow clear rules.

The formation energies of SACs and DACs were calculated to evaluate the structural stability, as shown in Figure S4. The formation energies of SACs (from−11.29 eV to −16.26 eV) is generally a little lower than those of DACs (from−7.53 eV to −15.58 eV), showing slightly higher structural stability than DACs. Fortunately, the apparently negative formation energies of DAC also suggest their favorable structural stability. Subsequently, we calculated the surface energies of six MnTMBNCs to clarify the distinctions in these 2D DACs' stability. Figure S5 illustrates MnCrBNC and MnFeBNC with the lowest surface energies, indicating enhanced stability in their structures.

To investigate the electronic structure interactions of the dual atoms in DACs, we calculated the *d*-orbital PDOSs of Mn and TM in MnTMBNC and then depicted them in Figure 1(c), along with their COHPs in Figure 1(d). As the number of *d*-orbital electrons in the TM increases, the overlap of the *d*-orbital PDOS between Mn and the TM atoms decreases. Moreover, the COHP results suggest a weakening of bonding between *d*−*d* orbitals, indicating a reduction in the strength of *d*-orbital interactions.

We examined the *d*-orbital interactions in DACs by comparing the *d*-orbital PDOSs of CrBNC, MnBNC, and MnCrBNC in Figure 2(a), with the optimized structures shown in Figure S6. Compared to CrBNC, MnCrBNC exhibits a significant rearrangement in the $d_{x^2-y^2}$ orbitals of Cr, leading to the formation of new bonding and antibonding orbitals. Similar changes were observed for the Mn atom, while the amount of empty $d_{x^2-y^2}$ orbital states above the Fermi level almost remains unchanged, which is beneficial for the reaction with lithium polysulfides as an electron acceptor. The PDOS of the other *d* orbitals shows minor fluctuations, indicating that the *d*−*d* orbital interactions primarily involve the $d_{x^2-y^2}$ orbitals. Additionally, we included PDOS calculations for MnBNC, CuBNC, and MnCuBNC to compare the interaction variances between Mn and various metals, illustrated in Figure S7. The Cu_d_{xy} orbital in MnCuBNC shifts above the Fermi level compared to CuBNC, suggesting electron transitions from Cu_d_{xy} orbital to other orbitals. On the other hand, the Mn_$d_{x^2-y^2}$ orbitals in MnCuBNC also split like those in MnCrBNC, while partial of the empty Mn_$d_{x^2-y^2}$ orbitals probably accept the electrons from Cu_d_{xy} orbitals and move to below the Fermi-level. Therefore, MnCuBNC is less reactive compared with MnCrBNC, and shows inferior catalytic and adsorption capability than MnCrBNC.

Furthermore, we calculated the ICOHP values for specific orbital interactions, including d_{xz}_d_{xz}, d_{yz}_d_{yz}, d_{z^2}_d_{z^2}, $d_{x^2-y^2}$_$d_{x^2-y^2}$, and d_{xy}_d_{xy} between Mn and various TM atoms (Table S1). The corresponding orbital interaction patterns are shown in Figure 2b and S8. The ICOHP values for the d_{yz}_d_{yz} and $d_{x^2-y^2}$_$d_{x^2-y^2}$ orbital interactions between the Cr and Mn atoms are−0.10 eV and−0.32 eV, respectively. In contrast, with the ICOHP values for the remaining *d*-orbital interactions are 0, indicating the *d*−*d* orbital interactions between the Cr and Mn atoms only involve the d_{yz} and $d_{x^2-y^2}$ orbitals. The ICOHP values for the $d_{x^2-y^2}$ orbital interactions in MnTMBNC (TM = Fe/Co/Ni) are−0.25 eV,−0.22 eV, and−0.14 eV, respectively, while all the other *d* orbitals have values of 0 eV. The discrepancy in ICOHP values in the $d_{x^2-y^2}$ orbital primarily arises from differences in the number of *d* electrons and energy level distinctions between Mn and the various TMs. In comparison, in MnTMBNC (TM = Cu/Zn), all *d*-orbital ICOHP values are 0, indicating very weak interactions among these *d*-orbitals between Mn and Cu/Zn atoms.

We conclude that the electronic interaction of the adjacent TM atoms primarily involves the interactions of their d_{xz}, d_{yz}, and $d_{x^2-y^2}$ orbitals. Based on the PDOS between MnCrBNC and MnCuBNC (Figure 2(a) and Figure S7), along with the bonding and antibonding orbital configurations of the *d* orbitals, we summarize the interaction diagram of d orbitals in Figure 2(c, d) and Figure S9. In the *d*-orbital interaction between Mn and TM, electron occupancy in the δ^* antibonding orbital impedes bonding, whereas the d_{yz} and $d_{x^2-y^2}$ orbitals establish stable π and σ bonding orbitals with paired electrons. Within the Mn−Fe/Co/Ni/Zn/Cu DAC system, the occupancy of electrons in the π^* and σ^* antibonding orbitals elevates the energy of the system, indicating less favorable *d*−*d* orbital interaction. In summary, the number of *d* electrons in DACs has a direct influence on the interactions between the d_{xz}, d_{yz}, and $d_{x^2-y^2}$ orbitals.

Due to the higher activity of the Cr/Mn site, we selected the MnCrBNC structure for further investigation into the dynamic stability of DACs. We conducted additional AIMD simulations with the canonical ensemble (NVT) for 10 ps on MnCrBNC, and Figure S10 illustrates energy and temperature variations over time. The energy and temperature quickly equilibrate and then exhibit slight fluctuation within 1 eV and 50 °C as the simulation progresses. Moreover, the MnCrBNC structure shows no significant distortion or bond breakage following a 10 ps dynamic simulation at 300 K, confirming its high structural stability.

3.2. Anchoring Performance. One of the most effective strategies to mitigate the detrimental shuttle effect involves confining lithium polysulfides (LiPSs) to the sulfur cathode. We explored the interactions between LiPSs (molecule structures depicted in Figure S11) and various substrates, including MnCrBNC, CrBNC, MnBNC, BNC, and BN. We illustrated the optimized adsorption configurations in Figure 3(a) and Figures S12−15, displayed the corresponding adsorption energies in Figure 3(b) and documented them in Table S2. It is noteworthy that Li_2S_n/S_8 molecules typically adsorb onto one metal site after geometry optimization, indicating a tendency of forming S−TM single bond. CrBNC and MnBNC exhibit adsorption energies for LiPSs ranging from 0.78 to 2.6 eV. In contrast, MnCrBNC demonstrates superior immobilization ability with adsorption energies ranging from 1.12 to 2.98 eV. Additionally, we observed that the vdW force contribution ratio (R_{vdW}) of adsorption energies in the MnCrBNC···Li_2S_n/S_8 configurations decreases as the number of S atoms increases, indicating an increasing ratio of chemical bonding. Furthermore, comparing the R_{vdW} in adsorption energies of Li_2S_n/S_8 on MnCrBNC with those on CrBNC or MnBNC (Figure S16), it is evident that the R_{vdW} values for MnCrBNC are lower. This suggests a higher contribution of chemical bonding for MnCrBNC adsorbing Li_2S_n/S_8 and its corresponding superior anchoring capability. Additionally, the R_{vdW} values of short chain LiPSs on CrBNC and MnBNC are relatively low, consistent with their stronger adsorption.

The charge density difference contours for MnCrBNC···Li_2S_n/S_8 configurations, illustrated in Figure S17, reveal intriguing patterns. We observed electron accumulation at the midpoint of the Li−N atom pair and the S−TM bond. The

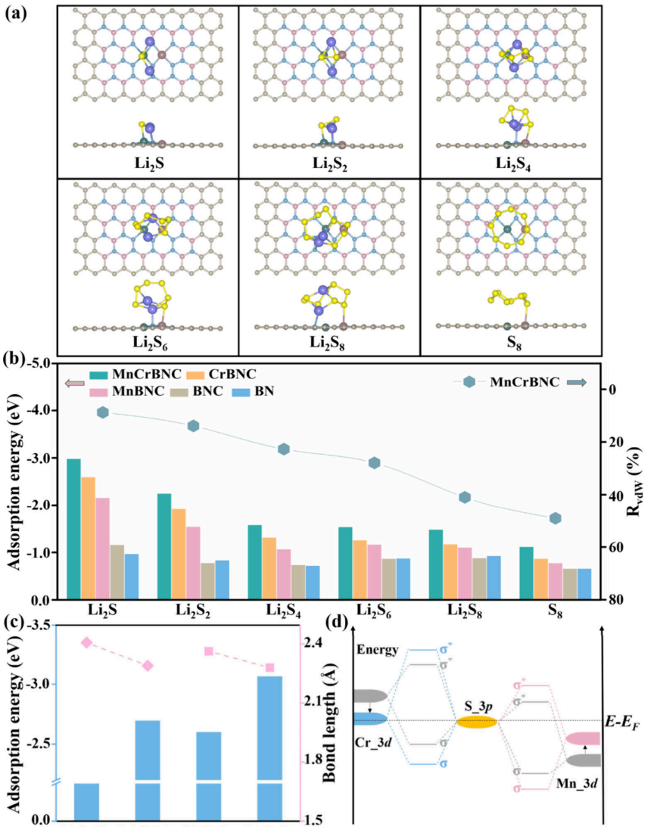

Figure 3. (a) Optimized structures of LiPSs adsorbed on MnCrBNC. (b) Adsorption energies in different configurations and the R_{vdW} of LiPSs on MnCrBNC. (c) Adsorption energies of Li_2S on two SACs (CrBNC and MnBNC) and two TM sites on the MnCrBNC DAC (DAC_Cr and DAC_Mn), and the corresponding S−Cr/Mn bond lengths. (d) Orbital interactions between Cr/Mn_3*d* orbitals in MnCrBNC and S_3*p* orbitals in Li_2S molecular. The asterisk "*" denotes the modulated orbital in DACs compared to SACs without asterisks.

bubble denoting electron accumulation between the Li−N atom pair is smaller than that associated with the S−TM bond, suggesting a more pronounced role of the S−TM bond in enhancing adsorption energy and mitigating the shuttle effect. However, we observed distinct interactions between the Li−N and S−TM atom pairs. The electron accumulation between the Li−N atom pair signifies a dipole−dipole interaction between lithium and nitrogen atoms.[43] In contrast, the S−TM bond exhibits an increase in electronic density around the S atom and a decrease around the TM atom, indicating the electron transfer from the TM atoms to the S atoms to form stable *σ* bonds.

To further elucidate the impact of electronic regulation through dual-atom interaction, we conducted a detailed investigation into the adsorption of Li_2S on two SACs (CrBNC and MnBNC, denoted as SAC_Cr and SAC_Mn) and two TM sites on the MnCrBNC DAC (denoted as DAC_Cr and DAC_Mn). Figure 3(c) presents the adsorption energies and the lengths of the resulting S−TM bonds, while the adsorption structures are depicted in Figure S18. The adsorption energies of Li_2S on SAC_Mn and DAC_Mn are 2.16 and 2.68 eV, with corresponding S−Mn bond lengths of 2.41 and 2.29 Å. Similarly, compared to SAC_Cr, DAC_Cr exhibited a 0.47 eV higher in adsorption energy and a 0.08 Å shorter S−Cr bond length, respectively. These results suggest that *d*-orbital interactions, a feature absent in SACs, a finding with practical implications in battery technology, activate the dual TM atoms in DACs. By combining the differential charge distribution results, we can conclude that the *σ* bond formed by the S_3p_z and Cr_3d_{z^2} orbital interaction significantly influences the strength of the S−Cr bond.

To elucidate the impact of *d*-band center on the binding energies of LiPSs, we calculated the energy band center difference between the 3*d* orbitals in CrBNC, MnBNC, CuBNC, MnCrBNC, MnCuBNC and the S_3p_z orbitals of Li_2S (Figure S19). The results demonstrated that the interaction of *d* orbitals in MnCrBNC decreases the energy band center difference (0.25 eV) between the Cr_3*d* and the S_3p_z orbitals, in contrast to that between the Cr_3*d* orbitals in CrBNC and the S_3p_z orbitals (0.48 eV). Similarly, the energy band center difference between the Mn_3*d* orbitals in MnCrBNC and the S_3p_z orbitals in LiPSs is reduced from 0.64 to 0.37 eV. The decreased energy band center differences between the Mn/Cr_3*d* orbitals and the S_3p_z orbitals enhance the interaction of MnCrBNC with LiPSs and the formed S−TM bonds. Conversely, the weaker hybridizations of d_{yz} and $d_{x^2-y^2}$ orbitals in MnCuBNC increase the energy band center difference between the Mn_3*d* and the S_3p_z orbitals by 0.37 eV, indicating weaker electronic interaction between MnCuBNC and LiPSs. The analysis of band center changes is consistent with the anchoring and catalytic performance analyses. Furthermore, Figure S20(a,b) depicts the PDOS for the Cr_3d_{z^2} and S_3*p* orbitals of CrBNC and MnCrBNC before and after bonding with Li_2S. Comparing the Cr_3d_{z^2} orbitals of CrBNC and MnCrBNC in the absence of adsorbed Li_2S with the S_3*p* orbitals of the isolated Li_2S reveals that the energies of the S_3p_z orbitals are closer to the Cr_3d_{z^2} in MnCrBNC than in CrBNC, facilitating the formation of a stable *σ* bond. Furthermore, the bond formed by the S_3p_z orbitals and the Cr_3d_{z^2} orbitals in MnCrBNC exhibits a more pronounced downward shift. Additionally, comparing the *d* orbitals of Mn in MnCrBNC and MnBNC, we see that the energy level of the Mn_3d_{z^2} orbital in MnCrBNC is closer to the S_3p_z orbital, also facilitating the formation of a more stable *σ* bond (Figure S20 (**c**, **d**)). The *d*-orbital interaction of the dual-atom in MnCrBNC shifts the 3d_{z^2} orbital closer to the energy level of the S_3p_z orbital, enhancing the S−TM bond, thereby improving anchoring performance (as shown in the schematic plot of Figure 3(d)).

3.3. Catalytic Performance Analysis.

The decomposition of Li_2S during the initial stage of the charging process is crucial for sulfur utilization and cycling stability of LSBs.[44] Figure 4(a) and Figure S21 show the top views of the Li_2S decomposition pathways. Figure 4(b) presents the average Li−S bond lengths of Li_2S adsorbed on various surfaces and the energy differences (E_d) before and after Li_2S decomposition. The decrease in energy difference accompanied by an increase in Li−S bond length generally suggests a reduction in the decomposition energy barrier. We observed that the energy barriers for Li_2S decomposition on MnCrBNC, CrBNC, and MnBNC are 1.25, 1.77, and 1.82 eV, respectively, as shown in Figure 4(c). The configuration of Li_2S adsorbed on MnCrBNC displays the longest Li−S bond length, the smallest energy difference, and the lowest energy barrier for Li_2S decomposition. In addition, the rapid migration of Li^+ can suppress the redeposition of Li_2S and facilitate the decomposition of Li_2S. We supplemented the energy barriers of Li^+ migration on

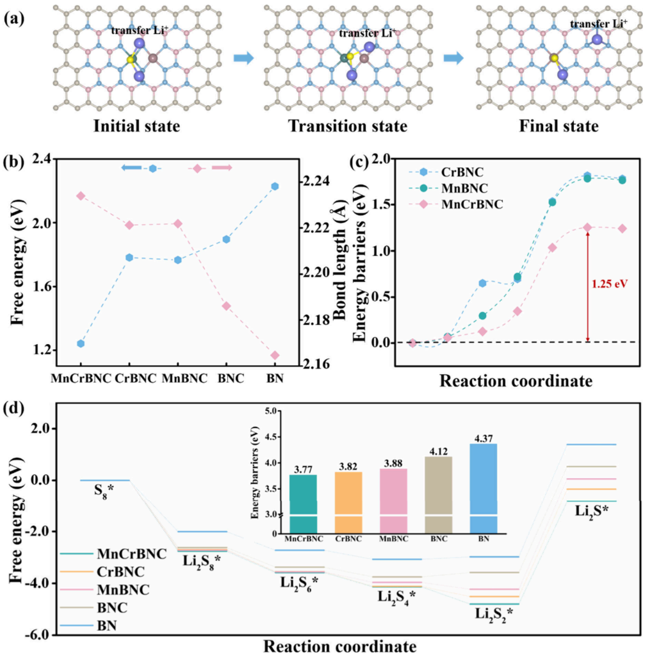

Figure 4. (a) Top view of the dissociation paths of Li_2S on the MnCrBNC. (b) Energy difference (E_d) between the initial and final states during the decomposition of Li_2S, along with the average Li−S bond length of Li_2S on various surfaces. (c) Decomposition energy barriers of the Li_2S adsorbed on CrBNC, MnBNC, and MnCrBNC. (d) Free-energy profiles for the S_8/LiPSs conversion on various surfaces (MnCrBNC, TiBNC, CuBNC, BNC, BN). The free energy of rate-determining steps are presented in the inset.

CrBNC, MnBNC, and MnCrBNC. The migration path is depicted in Figure S22, while the migration energy barriers are shown in Figure S23. The results demonstrate that the energy barrier of Li^+ MnCrBNC is the lowest (0.20 eV), indicating the incorporation of the Mn−Cr atom pair effectively decreases the migration energy barrier of Li^+ and facilitates the decomposition of Li_2S.

Another critical factor that restricts the high capacity and rate capability of LSBs is the slow kinetic process of LiPSs conversion during charging and discharging. By investigating the corresponding free energies based on eqs 6−11), the charging and discharging processes of the sulfur cathode involving multiple electrochemical reactions were further explored. The overall rate of these reactions depends on the rate-limiting step. Figure 4(d) shows the free energy profiles for the SRR process on various substrates, and Table S3 lists the corresponding free energies of reduction reactions. These values suggest that the overall SRR is exothermic. Among these steps, only the last step (reduction of Li_2S_2 to Li_2S) shows a positive change in free energy, indicating that the reduction of Li_2S_2 is the rate-determining step of SRR. Furthermore, incorporating metal atoms in DACs can effectively lower the ΔG of the rate-determining step. Compared to SACs, the MnCrBNC demonstrates a lower ΔG for the rate-determining step (3.77 eV), signifying its efficacy in facilitating the LiPSs transformations.

3.4. Feasibility Analysis. BNC combines the benefits of BN and graphene, enhancing battery safety with features like flame retardancy, toughness, and conductivity, thereby offering significant potential for battery applications. By adjusting the *d*-band center of the dual metal atoms in the BNC, the anchoring and catalytic properties of the DACs can be tailored. MnCrBNC demonstrates an enhanced adsorption energy strength on LiPSs compared to the current Ni−Co diatomic catalyst,[45] with a 0.5 eV increase, and a lower decomposition energy barrier for Li_2S, indicating the potential for improving battery performance. In terms of experimental feasibility, established experimental methods exist for synthesizing BNC, such as Ci et al.[34] synthesized BNC using chemical vapor deposition. Additionally, Niu et al.[46] synthesized ten distinct diatomic catalysts using a macrocyclic precursor-mediated approach, which can potentially be extended to the synthesis of the diatomic catalysts in this study.

4. CONCLUSIONS

We systematically investigated DACs with highly conductive BNC as the substrate for use as LSB host materials to mitigate the “shuttle effect” and accelerate the decomposition of Li_2S. Our research demonstrated that the *d*-band centers of DACs can be regulated by the adjacent TM atoms, primarily due to the number of electrons in the d_{yz} and $d_{x^2-y^2}$ orbitals. When DACs have ten or fewer *d* electrons, the d_{yz} and $d_{x^2-y^2}$ orbitals can form stable π and σ bonds, adjusting the *d*-band center for interaction with soluble LiPSs. Following this principle, MnCrBNC was selected for its superior LiPS anchoring and catalytic conversion capabilities compared to CrBNC and MnBNC. Our calculations indicate that MnCrBNC exhibits more favorable adsorption energy due to its regulated *d*-band center. Moreover, MnCrBNC facilitates the decomposition of Li_2S, demonstrating a lower energy barrier of 1.25 eV. From a thermodynamic perspective, MnCrBNC accelerates the multi-step SRR process by reducing the free energy of the reaction of the rate-limiting step. This research highlights the advantages of DACs, specifically MnCrBNC, and provides valuable insights into the strategic design of DACs as versatile materials for improving the performance of LSBs.

AUTHOR INFORMATION

Corresponding Authors

Qiu He – *College of Materials Synthesis and Engineering, Sichuan University, Chengdu 610065, China; Institute of Nanotechnology, Karlsruhe Institute of Technology, Eggenstein-Leopoldshafen 76344, Germany*; Email: hq5220@scu.edu.cn

Yan Xiong – *College of Mechanical Engineering, Sichuan University, Chengdu, Sichuan 610065, China*; Email: xy@scu.edu.cn

Yan Zhao – *The Institute of Technological Sciences, Wuhan University, Wuhan 430072, China; College of Materials Synthesis and Engineering, Sichuan University, Chengdu 610065, China*; orcid.org/0000-0002-1234-4455; Email: yanzhao@scu.edu.cn

Authors

Jianfeng Liu – *The Institute of Technological Sciences, Wuhan University, Wuhan 430072, China*

Wanjuan Zou – *Department of Mechanical and Aerospace Engineering, University of California, Irvine, California 92697, United States*

Mingwei Wu – *College of Materials Synthesis and Engineering, Sichuan University, Chengdu 610065, China*

Celso Ricardo Caldeira Rego – *Institute of Nanotechnology, Karlsruhe Institute of Technology, Eggenstein-Leopoldshafen 76344, Germany*; orcid.org/0000-0003-1861-2438

Chenxi Xia – *The Institute of Technological Sciences, Wuhan University, Wuhan 430072, China*

Notes

The authors declare no competing financial interest.

ACKNOWLEDGMENTS

This work was financially supported by the National Natural Science Foundation of China (22273096), the International Postdoctoral Exchange Fellowship Program between Helmholtz and OCPC (ZD2023019), and the Sichuan Provincial Natural Science Foundation for Young Scientists (24NSFSC6607).

REFERENCES

(1) Wang, P.; Xi, B. J.; Huang, M.; Chen, W. H.; Feng, J. K.; Xiong, S. L. Emerging Catalysts to Promote Kinetics of Lithium-Sulfur Batteries. *Adv. Energy Mater.* **2021**, *11* (7), 2002893.

(2) Wang, Y. C.; Chu, F. L.; Zeng, J.; Wang, Q. J.; Naren, T. Y.; Li, Y. Y.; Cheng, Y.; Lei, Y. P.; Wu, F. X. Single Atom Catalysts for Fuel Cells and Rechargeable Batteries: Principles, Advances, and Opportunities. *ACS Nano* **2021**, *15* (1), 210–239.

(3) Zhao, Q.; Zhu, Q. Z.; Liu, Y.; Xu, B. Status and Prospects of MXene-Based Lithium-Sulfur Batteries. *Adv. Funct. Mater.* **2021**, *31* (21), 2100457.

(4) Zhang, J.; You, C. Y.; Lin, H. Z.; Wang, J. Electrochemical Kinetic Modulators in Lithium-Sulfur Batteries: From Defect-Rich Catalysts to Single Atomic Catalysts. *Energy Environ. Mater.* **2022**, *5* (3), 731–750.

(5) Chen, Y.; Wang, T. Y.; Tian, H. J.; Su, D. W.; Zhang, Q.; Wang, G. X. Advances in Lithium-Sulfur Batteries: From Academic Research to Commercial Viability. *Adv. Mater.* **2021**, *33* (29), 2003666.

(6) Zhao, M.; Chen, X.; Li, X. Y.; Li, B. Q.; Huang, J. Q. An Organodiselenide Comediator to Facilitate Sulfur Redox Kinetics in Lithium-Sulfur Batteries. *Adv. Mater.* **2021**, *33* (13), No. e202303363.

(7) Mahato, M.; Nam, S.; Lee, M. J.; Koratkar, N.; Oh, I. Physicochemically Interlocked Sulfur Covalent Triazine Framework for Lithium-Sulfur Batteries with Exceptional Longevity. *Small* **2023**, *19* (30), 2301847.

(8) Manthiram, A.; Chung, S. H.; Zu, C. X. Lithium-Sulfur Batteries: Progress and Prospects. *Adv. Mater.* **2015**, *27* (12), 1980–2006.

(9) Gu, X. X.; Wang, Y. Z.; Lai, C.; Qiu, J. X.; Li, S.; Hou, Y. L.; Martens, W.; Mahmood, N.; Zhang, S. Q. Microporous bamboo biochar for lithium-sulfur batteries. *Nano Res.* **2015**, *8* (1), 129–139.

(10) Zhang, M.; Chen, W.; Xue, L. X.; Jiao, Y.; Lei, T. Y.; Chu, J. W.; Huang, J. W.; Gong, C. H.; Yan, C. Y.; Yan, Y. C.; Hu, Y.; Wang, X. F.; Xiong, J. Adsorption-Catalysis Design in the Lithium-Sulfur Battery. *Adv. Energy Mater.* **2020**, *10* (2), 1903008.

(11) Ng, S. F.; Lau, M. Y. L.; Ong, W. J. Lithium-Sulfur Battery Cathode Design: Tailoring Metal-Based Nanostructures for Robust Polysulfide Adsorption and Catalytic Conversion. *Adv. Mater.* **2021**, *33* (50), 2008654.

(12) Wang, J. Y.; Qiu, W. B.; Li, G. R.; Liu, J. B.; Luo, D.; Zhang, Y. G.; Zhao, Y.; Zhou, G. F.; Shui, L. L.; Wang, X.; Chen, Z. W. Coordinatively Deficient Single-atom Fe-N-C Electrocatalyst with Optimized Electronic Structure for High-performance Lithium-sulfur Batteries. *Energy Storage Mater.* **2022**, *46*, 269–277.

(13) Zhang, S. L.; Ao, X.; Huang, J.; Wei, B.; Zhai, Y. L.; Zhai, D.; Deng, W. Q.; Su, C. L.; Wang, D. S.; Li, Y. D. Isolated Single-Atom Ni-N-5 Catalytic Site in Hollow Porous Carbon Capsules for Efficient Lithium-Sulfur Batteries. *Nano Lett.* **2021**, *21* (22), 9691–9698.

(14) Lu, C.; Fang, R. Y.; Chen, X. Single-Atom Catalytic Materials for Advanced Battery Systems. *Adv. Mater.* **2020**, *32* (16), 1906548.

(15) Zhou, G. M.; Wang, S. Y.; Wang, T. S.; Yang, S. Z.; Johannessen, B.; Chen, H.; Liu, C. W.; Ye, Y. S.; Wu, Y. C.; Peng, Y. C.; Liu, C.; Jiang, S. P.; Zhang, Q. F.; Cui, Y. Theoretical Calculation Guided Design of Single-Atom Catalysts toward Fast Kinetic and Long-Life Li-S Batteries. *Nano Lett.* **2020**, *20* (2), 1252–1261.

(16) Zeng, Z. H.; Nong, W.; Li, Y.; Wang, C. X. Universal-Descriptors-Guided Design of Single Atom Catalysts toward Oxidation of Li2S in Lithium-Sulfur Batteries. *Adv. Sci.* **2021**, *8* (23), 2102809.

(17) Liu, J. F.; Lu, R. H.; Xiao, G. F.; Zhang, C. Y.; Zhao, K.; He, Q.; Zhao, Y. Trade-off effect of 3d transition metal doped boron nitride on anchoring polysulfides towards application in lithium-sulfur battery. *J. Colloid Interface Sci.* **2022**, *616*, 886–894.

(18) Li, Y. J.; Wu, J. B.; Zhang, B.; Wang, W. Y.; Zhang, G. Q.; Seh, Z. W.; Zhang, N.; Sun, J.; Huang, L.; Jiang, J. J.; Zhou, J.; Sun, Y. M. Fast conversion and controlled deposition of lithium (poly)sulfides in lithium-sulfur batteries using high-loading cobalt single atoms. *Energy Storage Mater.* **2020**, *30*, 250–259.

(19) Zhao, H.; Tian, B. B.; Su, C. L.; Li, Y. Single-Atom Iron and Doped Sulfur Improve the Catalysis of Polysulfide Conversion for Obtaining High-Performance Lithium-Sulfur Batteries. *ACS Appl. Mater. Interfaces* **2021**, *13* (6), 7171–7177.

(20) Yang, J.; Wang, Z. Y.; Huang, C. X.; Zhang, Y. D.; Zhang, Q. H.; Chen, C.; Du, J. Y.; Zhou, X.; Zhang, Y.; Zhou, H.; Wang, L. X.; Zheng, X. S.; Gu, L.; Yang, L. M.; Wu, Y. E. Compressive Strain Modulation of Single Iron Sites on Helical Carbon Support Boosts Electrocatalytic Oxygen Reduction. *Angew. Chem., Int. Ed.* **2021**, *60* (42), 22722–22728.

(21) Zhu, M. Z.; Zhao, C.; Liu, X. K.; Wang, X. L.; Zhou, F. Y.; Wang, J.; Hu, Y. M.; Zhao, Y. F.; Yao, T.; Yang, L. M.; Wu, Y. E. Single Atomic Cerium Sites with a High Coordination Number for Efficient Oxygen Reduction in Proton-Exchange Membrane Fuel Cells. *ACS Catal.* **2021**, *11* (7), 3923–3929.

(22) Zhao, M. R.; Song, B. Y.; Yang, L. M. Two-Dimensional Single-Atom Catalyst $TM_3(HAB)_2$ Monolayers for Electrocatalytic Dinitrogen Reduction Using Hierarchical High-Throughput Screening. *ACS Appl. Mater. Interfaces* **2021**, *13* (22), 26109–26122.

(23) Wang, X. L.; Yang, L. M. Unveiling the underlying mechanism of nitrogen fixation by a new class of electrocatalysts two-dimensional TM@g-C_4N_3 monosheets. *Appl. Surf. Sci.* **2022**, *576*, 151839.

(24) Li, R. Z.; Wang, D. S. Superiority of Dual-Atom Catalysts in Electrocatalysis: One Step Further Than Single-Atom Catalysts. *Adv. Energy Mater.* **2022**, *12* (9), 2103564.

(25) Chen, Y.; Lin, J.; Pan, Q.; Liu, X.; Ma, T. Y.; Wang, X. D. Inter-Metal Interaction of Dual-Atom Catalysts in Heterogeneous Catalysis. *Angew. Chem., Int. Ed.* **2023**, *62* (42), No. e202306469.

(26) Wang, J.; Zhao, C. X.; Liu, J. N.; Song, Y. W.; Huang, J. Q.; Li, B. Q. Dual-atom catalysts for oxygen electrocatalysis. *Nano Energy* **2022**, *104*, 107927.

(27) Wei, K. L.; Pan, K. H.; Qu, G. F.; Zhou, J. H. Customization from Single to Dual Atomic Sites for Efficient Electrocatalytic CO$_2$ Reduction to Value-added Chemicals. *Chem-Asian J.* **2023**, *18* (17), No. e202300498.

(28) Liu, J.; Xu, H. X.; Zhu, J. Q.; Cheng, D. J. Understanding the Pathway Switch of the Oxygen Reduction Reaction from Single- to Double-/Triple-Atom Catalysts: A Dual Channel for Electron Acceptance-Backdonation. *JACS Au* **2023**, *3* (11), 3031−3044.

(29) Hou, C. C.; Wang, H. F.; Li, C. X.; Xu, Q. From metal-organic frameworks to single/dual-atom and cluster metal catalysts for energy applications. *Energy Environ. Sci.* **2020**, *13* (6), 1658−1693.

(30) Zhang, N. Q.; Zhang, X. X.; Kang, Y. K.; Ye, C. L.; Jin, R.; Yan, H.; Lin, R.; Yang, J. R.; Xu, Q.; Wang, Y.; Zhang, Q. H.; Gu, L.; Liu, L. C.; Song, W. Y.; Liu, J.; Wang, D. S.; Li, Y. D. A Supported Pd-2 Dual-Atom Site Catalyst for Efficient Electrochemical CO2 Reduction. *Angew. Chem., Int. Ed.* **2021**, *60* (24), 13388−13393.

(31) Zeng, Z. P.; Gan, L. Y.; Yang, H. B.; Su, X. Z.; Gao, J. J.; Liu, W.; Matsumoto, H.; Gong, J.; Zhang, J. M.; Cai, W. Z.; Zhang, Z. Y.; Yan, Y. B.; Liu, B.; Chen, P. Orbital coupling of hetero-diatomic nickel-iron site for bifunctional electrocatalysis of CO$_2$ reduction and oxygen evolution. *Nat. Commun.* **2021**, *12* (1), DOI: 10.1038/s41467-021-24052-5.

(32) Zhang, L.; Si, R. T.; Liu, H. S.; Chen, N.; Wang, Q.; Adair, K.; Wang, Z. Q.; Chen, J. T.; Song, Z. X.; Li, J. J.; Banis, M. N.; Li, R. Y.; Sham, T. K.; Gu, M.; Liu, L. M.; Botton, G. A.; Sun, X. L. Atomic layer deposited Pt-Ru dual-metal dimers and identifying their active sites for hydrogen evolution reaction. *Nat. Commun.* **2019**, *10*, DOI: 10.1038/s41467-019-13466-x.

(33) Revabhai, P. M.; Singhal, R. K.; Basu, H.; Kailasa, S. K. Progress on boron nitride nanostructure materials: properties, synthesis and applications in hydrogen storage and analytical chemistry. *J. Nanostructure. Chem.* **2023**, *13*, 1−41.

(34) Ci, L.; Song, L.; Jin, C. H.; Jariwala, D.; Wu, D. X.; Li, Y. J.; Srivastava, A.; Wang, Z. F.; Storr, K.; Balicas, L.; Liu, F.; Ajayan, P. M. Atomic layers of hybridized boron nitride and graphene domains. *Nat. Mater.* **2010**, *9* (5), 430−435.

(35) Kresse, G; Hafner, J Norm-conserving and ultrasoft pseudopotentials for first-row and transition elements. *J. Phys.: Condens. Matter* **1994**, *6* (40), 8245.

(36) Kresse, G.; Furthmuller, J. Efficient iterative schemes for ab initio total-energy calculations using a plane-wave basis set. *Phys. Rev. B: Condens. Matter* **1996**, *54* (16), 11169−11186.

(37) Perdew, J. P.; Wang, Y. Accurate and simple analytic representation of the electron-gas correlation energy. *Phys. Rev. B: Condens. Matter* **1992**, *45* (23), 13244−13249.

(38) Perdew, J. P.; Burke, K.; Ernzerhof, M. Generalized gradient approximation made simple. *Phys. Rev. Lett.* **1996**, *77* (18), 3865−3868.

(39) Grimme, S.; Ehrlich, S.; Goerigk, L. Effect of the damping function in dispersion corrected density functional theory. *J. Comput. Chem.* **2011**, *32* (7), 1456−1465.

(40) Henkelman, G.; Uberuaga, B. P.; Jonsson, H. A climbing image nudged elastic band method for finding saddle points and minimum energy paths. *J. Chem. Phys.* **2000**, *113* (22), 9901−9904.

(41) Guan, W. J.; Cheng, W. W.; Pei, S. X.; Chen, X. B.; Yuan, Z. Q.; Lu, C. Probing Coordination Number of Single-Atom Catalysts by d-Band Center-Regulated Luminescence. *Angew. Chem., Int. Ed.* **2024**, *63* (16), No. e202401214.

(42) Tian, J. M.; Rao, Y.; Shi, W. H.; Yang, J. W.; Ning, W. J.; Li, H. Y.; Yao, Y. G.; Zhou, H. S.; Guo, S. H. Sabatier Relations in Electrocatalysts Based on High-entropy Alloys with Wide-distributed d-band Centers for Li-O2 Batteries. *Angew. Chem., Int. Ed.* **2023**, *62* (44), No. e20231089.

(43) Hou, T. Z.; Xu, W. T.; Chen, X.; Peng, H. J.; Huang, J. Q.; Zhang, Q. Lithium Bond Chemistry in Lithium-Sulfur Batteries. *Angew. Chem., Int. Ed.* **2017**, *56* (28), 8178−8182.

(44) Peng, L. L.; Wei, Z. Y.; Wan, C. Z.; Li, J.; Chen, Z.; Zhu, D.; Baumann, D.; Liu, H. T.; Allen, C. S.; Xu, X.; Kirkland, A. I.; Shakir, I.; Almutairi, Z.; Tolbert, S.; Dunn, B.; Huang, Y.; Sautet, P.; Duan, X. F. A fundamental look at electrocatalytic sulfur reduction reaction. *Nat. Catal.* **2020**, *3* (9), 762−770.

(45) Zhao, C.; Huo, F.; Yang, Y.; Ruan, J.; Chai, F.; Xu, H.; Liu, Y.; Zhang, L.; Cabot, A.; Sun, Z.; Zhang, Y. Development of Synergistically Efficient Ni−Co Pair Catalytic Sites for Enhanced Polysulfide Conversion in Lithium−Sulfur Batteries. *Adv. Funct. Mater.* **2024**, *34*, 2402175.

(46) Zhang, Y.-X.; Zhang, S.; Huang, H.; Liu, X.; Li, B.; Lee, Y.; Wang, X.; Bai, Y.; Sun, M.; Wu, Y.; Gong, S.; Liu, X.; Zhuang, Z.; Tan, T.; Niu, Z. General Synthesis of a Diatomic Catalyst Library via a Macrocyclic Precursor-Mediated Approach. *J. Am. Chem. Soc.* **2023**, *145* (8), 4819−4827.